Chapter

Materials Research on High-Entropy Alloy Superconductors

Jiro Kitagawa, Naoki Ishizu and Shusuke Hamamoto

Abstract

The first purpose of this chapter is materials research on face-centered-cubic (fcc) high-entropy alloy (HEA) superconductors, which have not yet been reported. We have investigated several Nb-containing multicomponent alloys. Although we succeeded in obtaining Nb-containing samples with the dominant fcc phases, no superconducting signals appeared in these samples down to 3 K. The microstructure analyses revealed that all samples were multi-phase, but the existence of several new Nb-containing HEA phases was confirmed in them. The second purpose is the report of materials research on the Mn_5Si_3-type HEA superconductors. This hexagonal structure offers various intermetallic compounds, which often undergo a superconducting state. The Mn_5Si_3-type HEA is classified into the multisite HEA, which possesses the high degree of freedom in the materials design and is good platform for studying exotic HEA superconductors. We have successfully found a single-phase Mn_5Si_3-type HEA, which, however, does not show a superconducting property down to 3 K. The attempt of controlling the valence electron count was not successful.

Keywords: high-entropy alloys, superconductivity, face-centered-cubic, niobium, Mn_5Si_3-type

1. Introduction

High-entropy alloys (HEAs) are a new class of materials and have attracted a great deal of attention [1, 2]. The concept of HEA was originally proposed for a face-centered-cubic (fcc), body-centered-cubic (bcc), or hexagonal-closed packing (hcp) structure. The most prominent feature of a HEA is that more than five elements, each having an atomic percentage between 5% and 35%, randomly occupy one crystallographic site (see also **Figure 1(a)**). This produces a large mixing entropy, and HEAs exhibit the combination of high yield strength and ductility [3], high strength at elevated temperatures [4], strong resistance to corrosion and oxidation [5], and so on. The high-entropy concept is extensively adapted in various materials such as oxides, chalcogenides, and halides [6, 7].

One of the novelties of HEAs is a cocktail effect, which indicates an enhancement of physical properties beyond the simple mixture of those of components. For example, several bcc HEAs show superior mechanical properties compared to conventional hard materials. Another example is found in magnetic spinel oxide $(Mg_{0.2}Co_{0.2}Ni_{0.2}Cu_{0.2}Zn_{0.2})Al_2O_4$. The high-entropy type spinel oxide interestingly

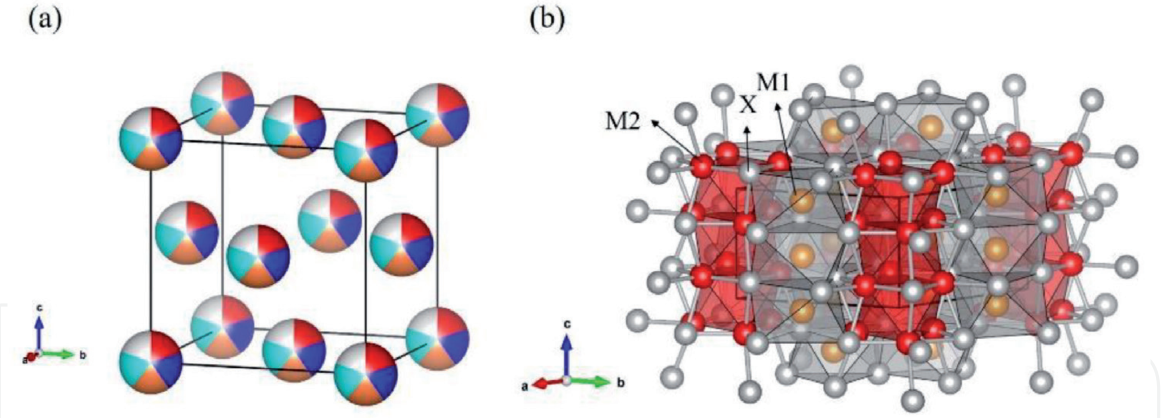

Figure 1.
Crystal structure of compounds with (a) fcc and (b) Mn_5Si_3-type structures. In (a), a multicolored ball means a random occupation by constituent elements.

shows enhanced magnetic frustration [8]. The cocktail effect is also reported in the structural stability of high-entropy-type materials. A γ-type disilicate structure is stable from room temperature to 1900°C in $(Gd_{1/6}Tb_{1/6}Dy_{1/6}Tm_{1/6}Yb_{1/6}Lu_{1/6})_2Si_2O_7$. The outstanding thermal stability is ascribed to the high-entropy state at the rare-earth site [9]. The other novelty of HEAs is the tuning of physical properties via the change of microstructure. The manufacturing process of HEAs considerably affects their microstructures, which are often deeply related to their physical properties. $Fe_{15}Co_{15}Ni_{20}Mn_{20}Cu_{30}$ shows a spinodal decomposition after the heat treatment [10]. The spinodally decomposed sample exhibits enhanced Curie temperature and magnetization compared to the homogenized single-phase sample. The tuning of magnetic properties is also reported in dual-phase HEAs [11–13].

One of the new research topics in HEA is the superconductivity found in 2014 [14]. Transition metal-based superconductors, forming simple crystalline structures, follow the so-called Matthias rule. When the superconducting critical temperature T_c is plotted as a function of valence electron count per atom (VEC), this rule shows broad peak structures at the specified VEC [15]. On the other hand, transition metal amorphous superconductors do not follow this rule and frequently show relatively high T_c values in the valley of the curve of the Matthias rule [16]. HEA superconductors with simple crystal structures have been found in bcc [17–22] and hcp [23–26]. The T_c vs. VEC plots of these HEAs seem to fall between a crystalline curve and an amorphous one [27, 28]. Thus, HEA superconductors will shed light on the study of the relationship between crystalline and amorphous compounds.

In the typical HEAs with fcc, bcc, or hcp structure, the superconductivity seems to appear in bcc or hcp HEAs. According to the classification by VEC, single-phase fcc HEA is stabilized for VEC larger than 8.0 [1, 2], where T_c would be substantially reduced in the VEC dependence of T_c observed in the Matthias rule. So it may be unrealistic to search for an fcc HEA superconductor. However, this is valuable to challenge because an fcc HEA superconductor would contribute to the deep understanding of HEA and/or the relationship between crystalline and amorphous compounds. In this chapter, we introduce our attempt at the search for an fcc HEA superconductor. Our strategy is to employ a rather high T_c element because the HEA superconductors reported to date contain superconducting elements [28]. We focused on the Nb-containing HEAs.

The concept of HEA is now used in superconducting materials with the crystal structures possessing multiple Wyckoff positions. For example, CsCl-type, α-Mn-type, A15, NaCl-type, σ-phase and $CuAl_2$-type HEA superconductors are reported

[29–37]. High degree-of-freedom in such a multisite HEA design would promote the investigations of multisite HEA superconductors. The second purpose of this chapter is the materials research on the hexagonal Mn_5Si_3-type HEAs, possessing multiple Wyckoff positions. Recently, several superconductors with the Mn_5Si_3-type—or its ordered derivative Ti_5Ga_4-type—structure have been found and attract much attention [38–44]. Besides, many intermetallic compounds are crystallizing into these crystal structures [45, 46]. **Figure 1(b)** shows the crystal structure of the Mn_5Si_3-type compound represented by M_5X_3. The space group is $P6_3/mcm$, and the M atoms occupy the $4d$ (for M1 atom) and $6g$ (for M2 atom) Wyckoff positions and the X atom another $6g$ one. The M2 atoms form a face-sharing octahedral chain along the c-axis. The X atoms also form another octahedron, which encloses the M1 atom forming a one-dimensional atomic chain along the c-axis.

In this chapter, we report the synthesis and characterization of the fcc and the Mn_5Si_3-type HEA samples. The measurement of AC magnetic susceptibility checked the superconducting state. We also present the phase analyses of both kinds of samples. Finally, the future direction of materials research on superconducting HEAs is mentioned.

2. Materials and methods

All samples were synthesized by a home-made arc furnace in an Ar atmosphere. The constituent elements as listed in **Table 1** were arc-melted on a water-cooled Cu hearth. The samples were turned over and melted several times. The Mn_5Si_3-type HEAs were annealed at 800°C for four days in evacuated quartz tubes.

A powder X-ray diffractometer (XRD-7000 L, Shimadzu, Kyoto, Japan) with Cu-Kα radiation was employed to detect the X-ray diffraction (XRD) patterns of

Element	Supply company	Purity (%)	Crystal structure	Atomic radius (Å)	VEC
Zr	Soekawa Chemicals, Tokyo, Japan	99	A3 (hcp)	1.6025	4
Nb	Nilaco, Tokyo, Japan	99.9	A2 (bcc)	1.429	5
V	Kojundo Chemical Laboratory, Sakado, Japan	99.9	A2 (bcc)	1.316	5
Ru	Soekawa Chemicals, Tokyo, Japan	99.9	A3 (hcp)	1.3384	8
Ir	Furuya Metal, Tokyo, Japan	99.99	A1 (fcc)	1.3573	9
Rh	Soekawa Chemicals, Tokyo, Japan	99.9	A1 (fcc)	1.345	9
Pd	Tanaka Kinzoku Kogyo, Tokyo, Japan	99.9	A1 (fcc)	1.3754	10
Cu	Soekawa Chemicals, Tokyo, Japan	99.99	A1 (fcc)	1.278	11
Sc	Furuya Metal, Tokyo, Japan	99.9	A3 (hcp)	1.641	3
Ti	Nilaco, Tokyo, Japan	99.9	A3 (hcp)	1.4615	4
Ga	Kojundo Chemical Laboratory, Sakado, Japan	99.99	A11	1.392	3
Si	Soekawa Chemicals, Tokyo, Japan	99.999	A4	1.153	4
Ge	Soekawa Chemicals, Tokyo, Japan	99.999	A4	1.24	4
Pt	Tanaka Kinzoku Kogyo, Tokyo, Japan	99.9	A1 (fcc)	1.387	10

Table 1.
Materials used in this study. The supply company, purity, crystal structure at room temperature, atomic radius [47], and VEC are also listed.

prepared samples. The microstructure of each sample was examined by a field emission scanning electron microscope (FE-SEM, JSM-7100F; JEOL, Akishima, Japan). The atomic compositions of the samples were checked by an energy dispersive X-ray (EDX) spectrometer equipped to the FE-SEM.

To confirm the diamagnetic signal due to the superconducting state, the temperature dependence of the AC magnetic susceptibility χ_{ac} (T) was measured by a home-made system in a GM refrigerator (UW404, Ulvac cryogenics, Kyoto, Japan) between 3 and 300 K. The amplitude and the frequency of the AC field were 5 Oe and 800 Hz, respectively.

3. Results and discussion

3.1 Nb-containing fcc HEAs

The starting compositions of prepared Nb-containing samples were determined, considering the conventional design rule [1, 2]: a δ-value less than 5% and a VEC larger than 8.0. To realize the requirements, fcc elements were predominantly used (see also **Tables 1** and **2**). The parameters of δ and VEC were calculated as follows:

No.	Sample	Composition of Phase I, II or III	δ	VEC
1	$Cu_{20}Nb_{15}Pd_{25}Rh_{30}V_{10}$		3.52	8.65
	Phase I	$Cu_{8.3(8)}Nb_{21.2(8)}Pd_{21.6(4)}Rh_{42.9(5)}V_{6.0(5)}$	3.14	8.29
	Phase II	$Cu_{14.4(5)}Nb_{12.6(5)}Pd_{28(1)}Rh_{26.4.(8)}V_{18.6(5)}$	3.26	8.32
	Phase III	$Cu_{65(5)}Nb_{2(1)}Pd_{28(2)}Rh_{2(1)}V_{3(1)}$	3.56	10.38
2	$Cu_{21}Ir_{21}Nb_{15}Pd_{22}Rh_{21}$		3.45	9.04
	Phase I	$Cu_{1.4(6)}Ir_{36.4(8)}Nb_{24.3(4)}Pd_{10.1(9)}Rh_{27.8(3)}$	2.52	8.16
	Phase II	$Cu_{8.5(7)}Ir_{6(1)}Nb_{12.5(6)}Pd_{46(3)}Rh_{27(2)}$	2.66	9.13
	Phase III	$Cu_{40(5)}Nb_{4(1)}Pd_{52(3)}Rh_{4(1)}$	3.74	10.16
3	$Cu_{21}Nb_{15}Pd_{22}Rh_{21}Zr_{21}$		8.00	7.99
	Phase I	$Cu_{19.3(3)}Pd_{37.2(2)}Rh_{19.2(4)}Zr_{24.3(5)}$	8.30	8.54
	Phase II	$Cu_{7(1)}Nb_{41(1)}Pd_{8(1)}Rh_{27(1)}Zr_{17(1)}$	6.60	6.73
	Phase III	$Cu_{57(1)}Pd_{13(1)}Rh_{9(1)}Zr_{21(1)}$	9.33	9.22
4	$Cu_{20}Nb_{15}Pd_{24}Rh_{25}V_{10}Zr_{6}$		5.62	8.34
	Phase I	$Cu_{14.5(3)}Nb_{15.7(5)}Pd_{31(1)}Rh_{23.1(5)}V_{7(1)}Zr_{8.7(5)}$	5.98	8.26
	Phase II	$Cu_{15.0(5)}Nb_{24(1)}Pd_{18(1)}Rh_{27.2(5)}V_{15.8(8)}$	3.72	7.89
	Phase III	$Cu_{86(1)}Pd_{14(1)}$	2.62	10.86
5	$Cu_{40}Nb_{20}Pd_{30}V_{10}$		4.44	8.9
	Phase I	$Cu_{21.1(2)}Nb_{27.6(2)}Pd_{39.7(7)}V_{11\,5(7)}$	4.05	8.25
	Phase II	$Cu_{89.2(5)}Pd_{10.8(5)}$	2.35	10.89
6	$Ir_{10}Nb_{17}Pd_{33}Rh_{28}Ru_{12}$		2.21	8.54
	Phase I	$Ir_{15.5(2)}Nb_{17.7(8)}Pd_{20.3(7)}Rh_{29.7(2)}Ru_{16.8(5)}$	2.30	8.33
	Phase II	$Ir_{4.0(6)}Nb_{16.0(5)}Pd_{51(1)}Rh_{22(1)}Ru_{7.0(7)}$	2.02	8.8

Table 2.
δ and VEC of Nb-containing samples and phases detected by EDX measurements.

$$\delta = 100 \times \sqrt{\sum_{i=1}^{n} c_i \left(1 - \frac{r_i}{\bar{r}}\right)^2} \tag{1}$$

and

$$VEC = \sum_{i=1}^{n} c_i VEC_i, \tag{2}$$

where c_i, r_i, and VEC_i are the atomic fraction, the atomic radius, and the VEC of element i, respectively, and $\bar{r}$ is the composition-weighted average atomic radius. The parameter δ means the degree of the atomic size difference among the constituent elements. The calculated parameters for the prepared samples are listed in **Table 2**, in which the samples are named as their starting compositions. $Cu_{20}Nb_{15}Pd_{25}Rh_{30}V_{10}$, $Cu_{21}Ir_{21}Nb_{15}Pd_{22}Rh_{21}$ and $Ir_{10}Nb_{17}Pd_{33}Rh_{28}Ru_{12}$ fulfill the design requirements. To investigate the effect of larger δ values, two samples, including a Zr atom, were prepared.

Shown in **Figure 2** is the XRD patterns of prepared samples. In the upper five samples, all containing Nb, Pd, and Cu atoms, $Cu_{20}Nb_{15}Pd_{25}Rh_{30}V_{10}$ and $Cu_{21}Ir_{21}Nb_{15}Pd_{22}Rh_{21}$ possess dominant fcc phases. On the other hand, the XRD patterns of Zr-containing samples ($Cu_{21}Nb_{15}Pd_{22}Rh_{21}Zr_{21}$ and $Cu_{20}Nb_{15}Pd_{24}Rh_{25}V_{10}Zr_6$) cannot be characterized by fcc phases. These results suggest that Zr is unfavorable for the formation of an fcc structure. In order to further investigate the formation condition of the single fcc phase, the quaternary alloy $Cu_{40}Nb_{20}Pd_{30}V_{10}$ was synthesized. As shown in **Figure 2**, this sample exhibits two fcc phases with quite different lattice parameters. The XRD pattern of the sample with no Cu atom

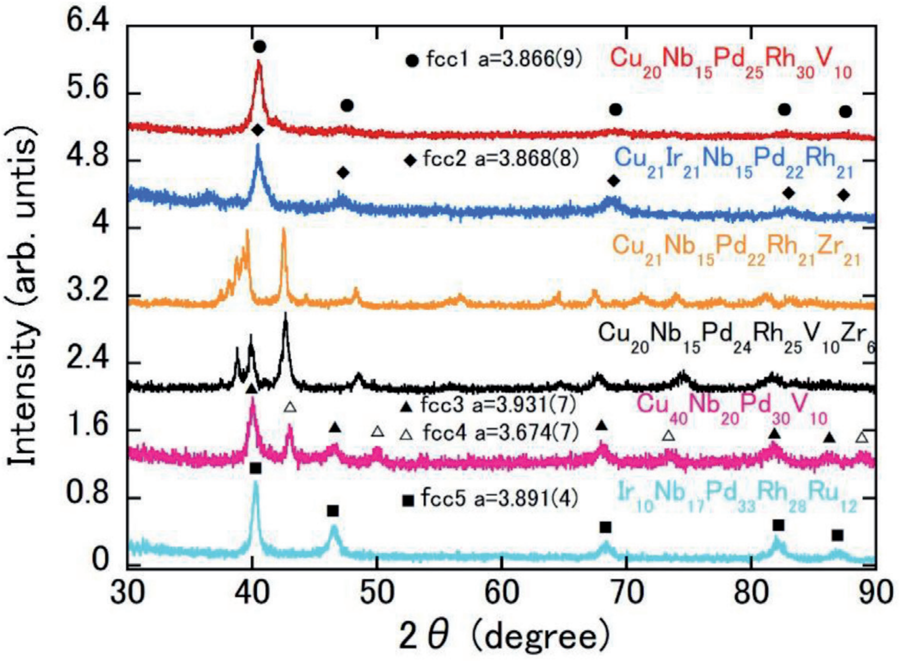

Figure 2.
XRD patterns of Nb-containing samples. The origin of each pattern is shifted by an integer value.

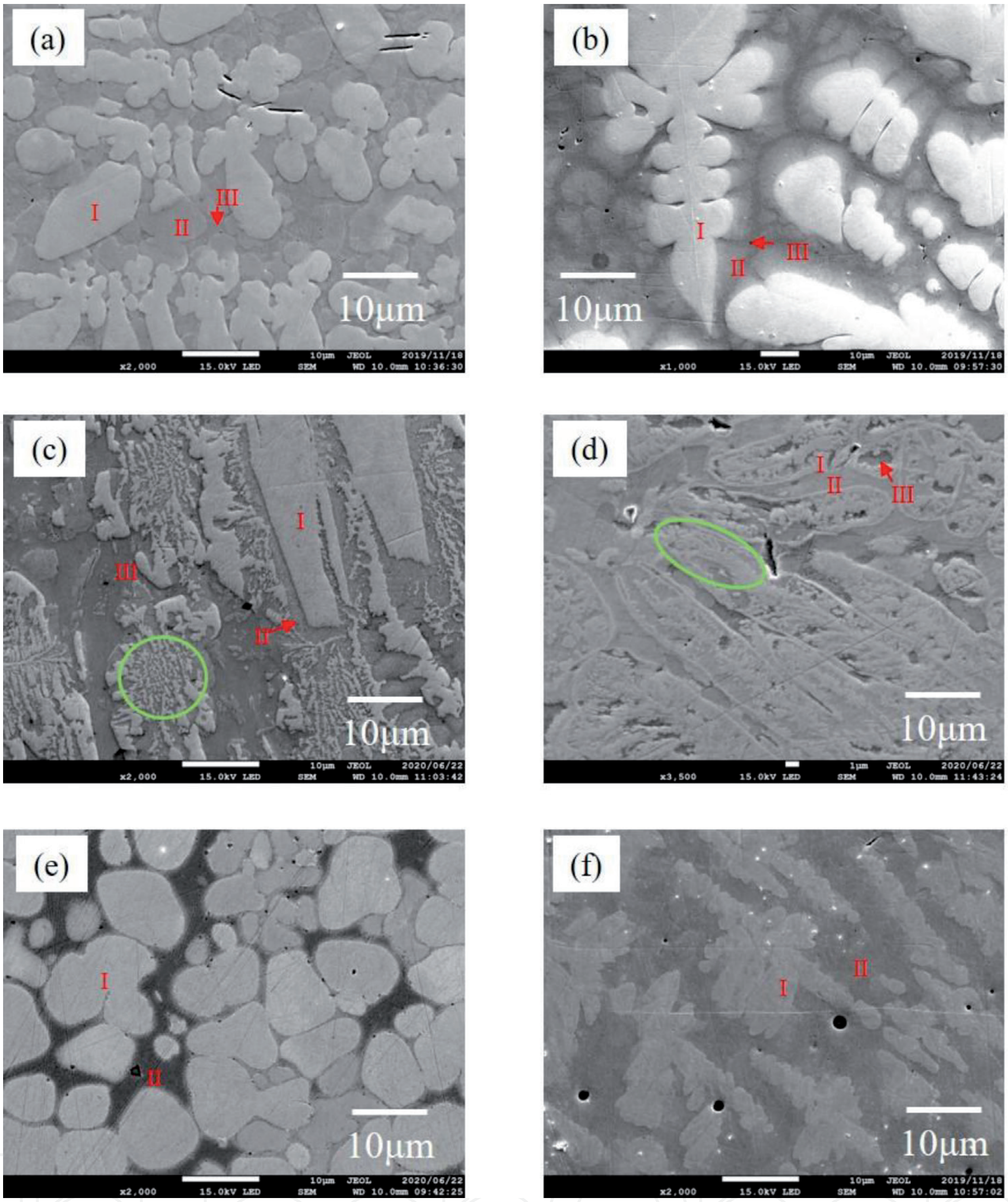

Figure 3.
Back-scattered electron (15 keV) images of (a) $Cu_{20}Nb_{15}Pd_{25}Rh_{30}V_{10}$, *(b)* $Cu_{21}Ir_{21}Nb_{15}Pd_{22}Rh_{21}$, *(c)* $Cu_{21}Nb_{15}Pd_{22}Rh_{21}Zr_{21}$, *(d)* $Cu_{20}Nb_{15}Pd_{24}Rh_{25}V_{10}Zr_{6}$, *(e)* $Cu_{40}Nb_{20}Pd_{30}V_{10}$, *and (f)* $Ir_{10}Nb_{17}Pd_{33}Rh_{28}Ru_{12}$, *respectively.*

(see the bottom of **Figure 2**) can be explained by an fcc phase. The lattice parameters of all fcc phases were obtained by the least-square method [48, 49] and are shown in **Figure 2**.

Figures 3(a)–(f) display the SEM images of samples, all indicating multi-phases. In $Cu_{20}Nb_{15}Pd_{25}Rh_{30}V_{10}$ (**Figure 3(a)**) and $Cu_{21}Ir_{21}Nb_{15}Pd_{22}Rh_{21}$ (**Figure 3(b)**), three contrast phases I, II and III were detected. In each case, the brightest area (phase I) showed a dendritic morphology, which is surrounded by phase II with the median contrast. The darkest area (phase III) would be the precipitate that formed in the final solidification process. A part of $Cu_{21}Nb_{15}Pd_{22}Rh_{21}Zr_{21}$ (**Figure 3(c)**) or $Cu_{20}Nb_{15}Pd_{24}Rh_{25}V_{10}Zr_{6}$ (**Figure 3(d)**) showed a eutectic-like structure formed by phase I and phase II (see, for example, the green elliptic closed-curve). As shown in **Figure 3(e)**, $Cu_{40}Nb_{20}Pd_{30}V_{10}$ possesses two phases, both of which would be fcc phases taking into account the XRD results. $Ir_{10}Nb_{17}Pd_{33}Rh_{28}Ru_{12}$ displays two contrast areas (see phases I and II in **Figure 3(f)**). The shape of the main phase has a dendritic-like morphology. The compositions of all phases determined by EDX are listed in **Table 2**.

χ_{ac} (T) measurements of all prepared samples suggested no superconductivity down to 3 K, which means that a Nb-containing fcc-HEA might be an inadequate strategy for searching fcc HEA superconductors. The appearance of superconductivity in a Nb-containing fcc compound might be a rare event because almost all Nb-based superconductors form bcc-related structures. NbN or NbC superconductor is a rare example, crystallizing into a NaCl-type structure related to the fcc structure [50, 51]. Although our results would be negative for the research of Nb-containing fcc HEA superconductors, it is to be noted that phase II in sample no. 1, phase I in sample no. 6 and possibly phases I and II in sample no. 4 are new members of HEA.

Here, we discuss the fcc phase stability, viewed from the parameters of δ and VEC, which is summarized in **Table 2**. We also calculate these parameters for the phases detected by EDX. The values of δ were very large in $Cu_{21}Nb_{15}Pd_{22}Rh_{21}Zr_{21}$ and $Cu_{20}Nb_{15}Pd_{24}Rh_{25}V_{10}Zr_6$ due to the larger atomic radius of Zr, which would lead to no fcc phase in each sample. While δ is reduced in $Cu_{20}Nb_{15}Pd_{25}Rh_{30}V_{10}$ and $Cu_{21}Ir_{21}Nb_{15}Pd_{22}Rh_{21}$, each sample shows three phases, all with rather low δ values. In each case, going from phase I to phase III, the VEC value increases, which accompanies the decrease (increase) of the Nb (Cu) atomic fraction. This suggests that the combination of Nb and Cu is not recommended even with a reduced δ, because an Nb-rich phase and a Cu-rich phase are stabilized for a smaller VEC and a larger VEC, respectively. Probably due to this reason, quaternary $Cu_{40}Nb_{20}Pd_{30}V_{10}$ does not show a single fcc phase. We note here that the addition of Cu leads to the breakdown of single-phase fcc CoCrFeNi into two fcc phases. This is ascribed to the positive enthalpy of mixing between the Cu and several elements [52]. $Ir_{10}Nb_{17}Pd_{33}Rh_{28}Ru_{12}$ with substantially suppressed δ and no Cu atom was expected to show a single fcc phase; however, two phases were detected in the sample. The detected phases possess reduced δ values and a similar VEC. Thus, it may not be easy to synthesize a single-phase Nb-containing fcc HEA.

No.	Sample	Composition of main phase	Composition of minor phase	VEC
1	(NbScTiVZr)(GaGeSi)	$(Nb_{13.0(1)}SC_{15.5(1)}Ti_{11.2(1)}V_{4.6(2)}Zr_{19.0(1)})(Ga_{4.4(2)}Ge_{19.3(1)}Si_{13.1(1)})$	$Ga_{7(1)}Ge_{6(1)}Nb_{19(1)}Sc_{8(1)}$ $Si_{7(1)}Ti_{17(1)}V_{28(1)}Zr_{8(1)}$	4
2	$(Nb_{1.25}Sc_{1.25}Ti_{1.25}Zr_{1.25})$ $(Ge_{1.8}Si_{1.2})$	$(Nb_{17(1)}Sc_{14(1)}Ti_{16(1)}Zr_{17(1)})$ $(Ge_{22(1)}Si_{14(1)})$	—	4
3	$(Nb_{1.25}Sc_{1.25}Ti_{1.25}Zr_{1.25})$ $(Ge_{1.55}Ru_{0.47}Si_{0.98})$	$(Nb_{18.0(2)}Sc_{13.5(4)}Ti_{12.3(5)}Zr_{20.5(6)})$ $(Ge_{21.4(2)}Si_{14.3(4)})$	$Nb_{28(4)}Ru_{31(4)}Sc_{6(2)}T_{31(3)}Zr_{4(1)}$	4.234
4	$(Nb_{1.4}ScTiZr_{1.6})$ $(Ge_{1.6}Pt_{0.3}Si_{1.1})$	$(Nb_{20.8(3)}Sc_{8.4(5)}Ti_{10.9(3)}Zr_{24(1)})$ $(Ge_{19.9(5)}Pt_{1.0(4)}Si_{15.0(5)})$	$Ge_{5.5(7)}Sc_{37(2)}Si_{1.7(2)}Ti_{15(1)}Pt_{40.7(7)}$	4.275
5	$(Nb_{1.4}ScTiZr_{1.6})$ $(Ge_{1.6}Ir_{0.3}Si_{1.1})$	$(Nb_{20.4(2)}Sc_{8.9(5)}Ti_{10.9(1)}Zr_{24.5(4)})$ $(Ge_{20.3(3)}Si_{15.0(2)})$	$Ge_{5.3(5)}Ir_{27.7(9)}Nb_{9.3(5)}Sc_{20.5(9)}Si_{4.0(6)}Ti_{16.4(5)}Zr_{16.7(8)}$	4.238

Table 3.
Chemical compositions of phases detected by EDX measurements for Mn_5Si_3-type HEA samples. VEC of each starting composition is also shown.

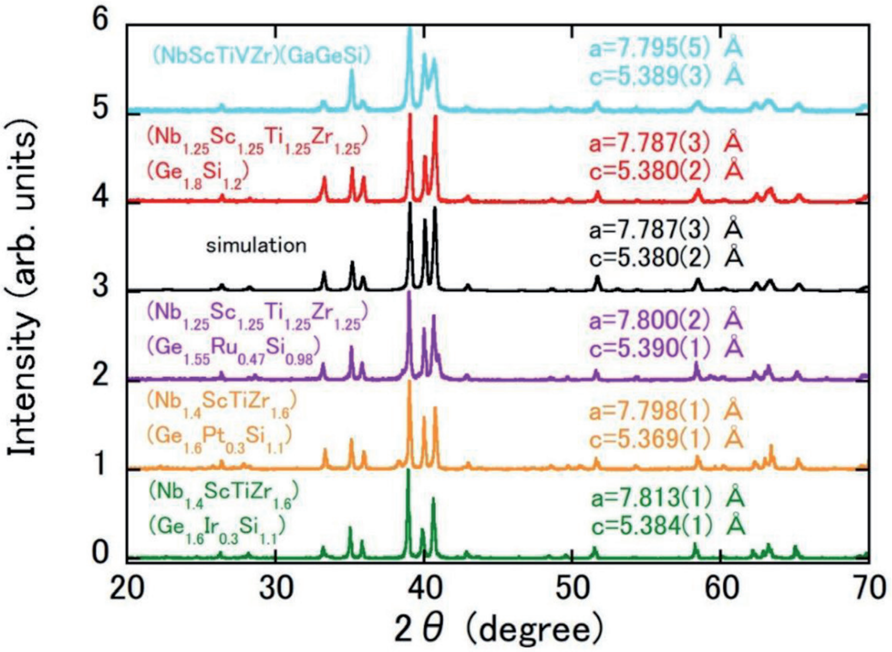

Figure 4.
XRD patterns of Mn_5Si_3*-type HEAs. The simulation pattern is also shown. Each pattern is shifted by an integer value for clarity.*

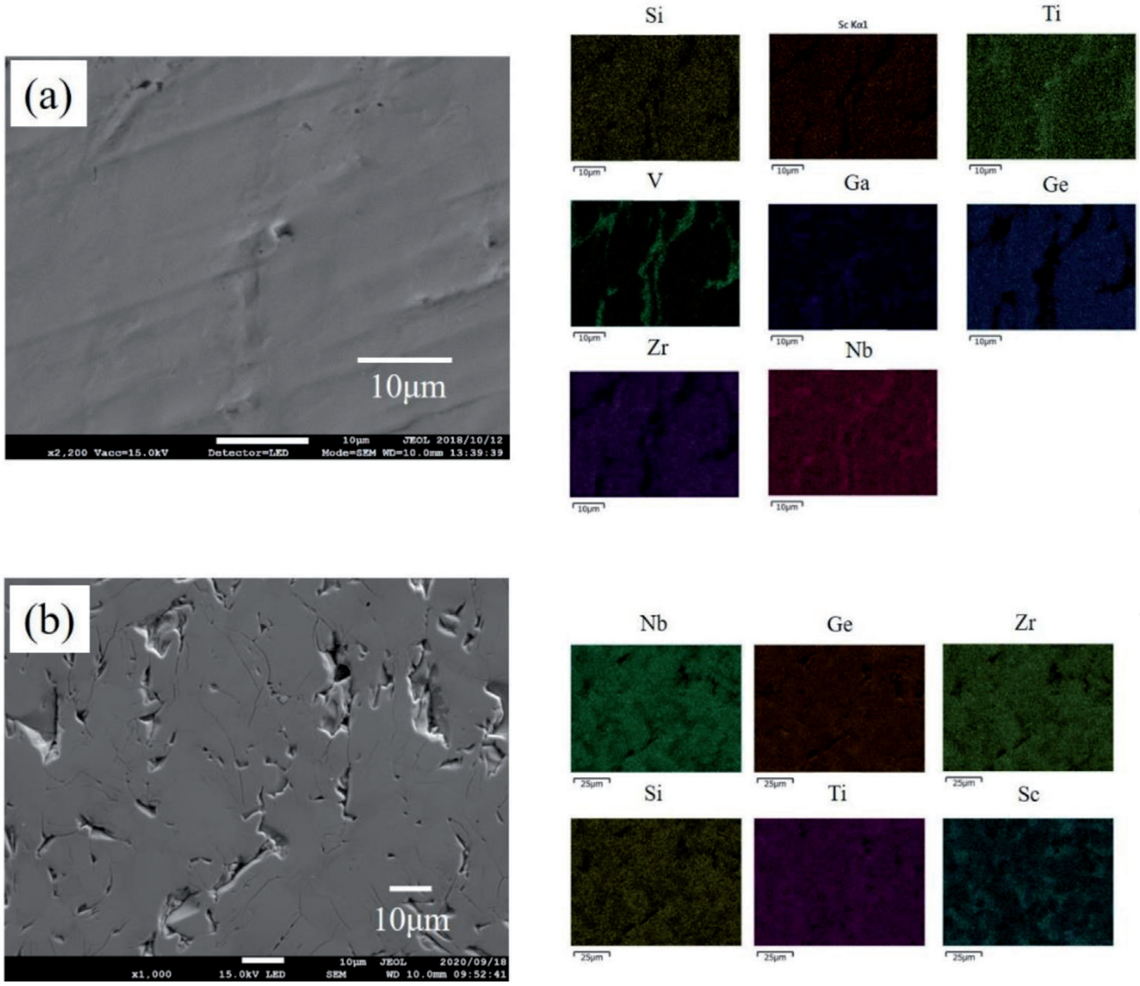

Figure 5.
Back-scattered electron (15 keV) images of (a) (NbScTiVZr)(GaGeSi), and (b) $(Nb_{1.25}Sc_{1.25}Ti_{1.25}Zr_{1.25})(Ge_{1.8}Si_{1.2})$*, respectively. The elemental mappings are also shown.*

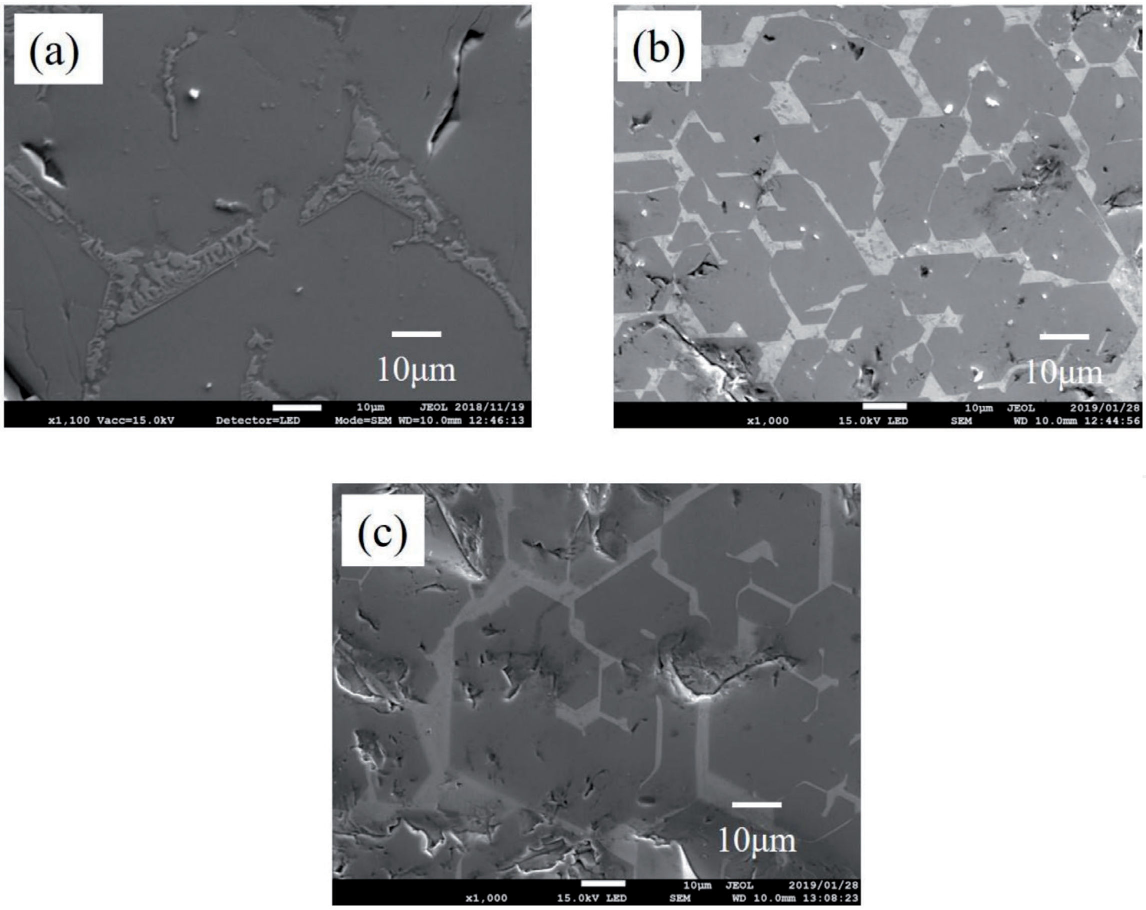

Figure 6.
Back-scattered electron (15 keV) images of (a) $(Nb_{1.25}Sc_{1.25}Ti_{1.25}Zr_{1.25})(Ge_{1.55}Ru_{0.47}Si_{0.98})$, *(b)* $(Nb_{1.4}ScTiZr_{1.6})(Ge_{1.6}Pt_{0.3}Si_{1.1})$, *and (c)* $(Nb_{1.4}ScTiZr_{1.6})(Ge_{1.6}Ir_{0.3}Si_{1.1})$, *respectively.*

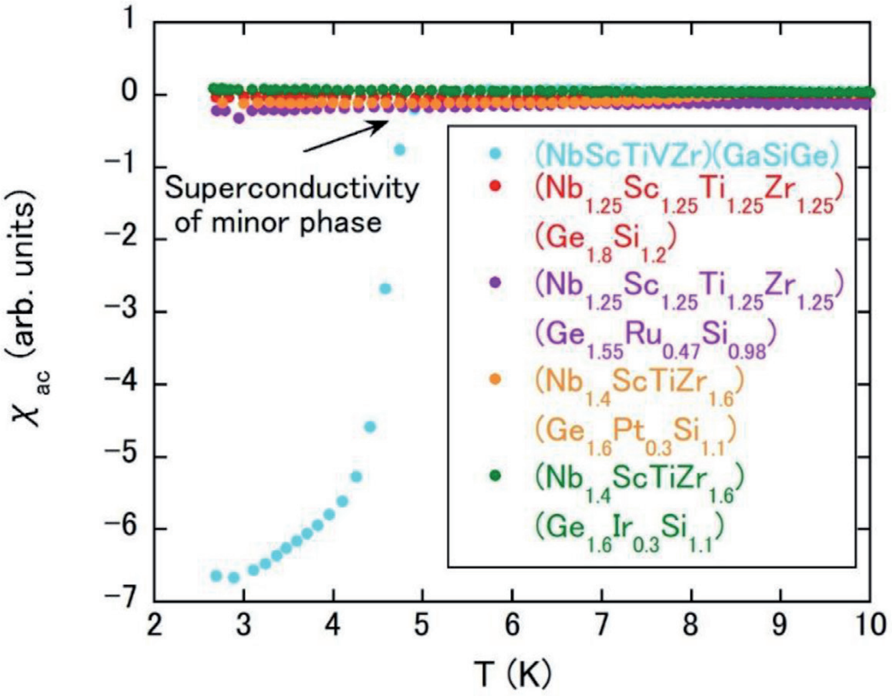

Figure 7.
Temperature dependences of χ_{ac} *of* Mn_5Si_3*-type HEA samples.*

3.2 Mn_5Si_3-type HEAs

We have prepared five Mn_5Si_3-type HEAs as listed in **Table 3**, and the XRD patterns are given in **Figure 4**. All XRD patterns are well indexed by the hexagonal Mn_5Si_3-type structure, and the determined lattice parameters are displayed in **Figure 4**. The SEM images of all samples are presented in **Figures 5** and **6**, and χ_{ac} (T) of each sample is shown in **Figure 7**.

We have started from (NbScTiVZr)(GaGeSi), which shows a diamagnetic signal (see **Figure 7**). However, as shown in **Figure 5(a)**, the elemental mapping has revealed the inhomogeneous distribution of constituent elements, which is obviously signaled by the V atom. The atomic compositions determined by EDX are $(Nb_{13.0(1)}Sc_{15.5(1)}Ti_{11.2(1)}V_{4.6(2)}\ Zr_{19.0(1)})(Ga_{4.4(2)}Ge_{19.3(1)}Si_{13.1(1)})$ for the V-poor phase and $Ga_{7(1)}Ge_{6(1)}Nb_{19(1)}Sc_{8(1)}Si_{7(1)}Ti_{17(1)}V_{28(1)}\ Zr_{8(1)}$ for the V-rich phase, respectively. The separately synthesized latter phase crystallizes into a bcc structure. This compound also shows the diamagnetic signal at approximately 5 K, which is identical to that of (NbScTiVZr)(GaGeSi). Therefore, (NbScTiVZr)(GaGeSi) would be an intrinsically normal state down to 3 K. The result of the chemical composition of the Mn_5Si_3-type phase in (NbScTiVZr)(GaGeSi) suggests the difficulty of incorporation of V and Ga atoms in a Mn_5Si_3-type HEA. Taking into account this experimental result, we have synthesized $(Nb_{1.25}Sc_{1.25}Ti_{1.25}Zr_{1.25})(Ge_{1.8}Si_{1.2})$. As shown in **Figure 4**, the sample is almost single phase, which is also supported by homogeneous elemental mapping (see also **Figure 5(b)**). The determined atomic composition is $(Nb_{17(1)}Sc_{14(1)}Ti_{16(1)}Zr_{17(1)})(Ge_{22(1)}Si_{14(1)})$, which agrees well with the starting composition. While the single-phase Mn_5Si_3-type HEA is successfully obtained, the diamagnetic signal cannot be confirmed down to 3 K, as shown in **Figure 7**.

One of the conceivable reasons for no superconductivity in the samples mentioned above is that the VEC value is slightly less than the optimal value (see also **Table 3**). As pointed out in the review [28], multisite HEA superconductors follow the respective Matthias rule, which means the important role of the density of states at the Fermi level. The VEC values of Mn_5Si_3-type superconductors Zr_5Sb_3 and $Zr_5Ge_{2.5}Ru_{0.5}$ are 4.375 and 4.25, respectively [40, 42], while the VEC value of (NbScTiVZr)(GaGeSi) or $(Nb_{1.25}Sc_{1.25}Ti_{1.25}Zr_{1.25})(Ge_{1.8}Si_{1.2})$ is 4. Thus, aiming at increasing the VEC, we substituted Ru, Pt, or Ir atoms at the Si site of Mn_5Si_3-type HEA. The prepared samples were $(Nb_{1.25}Sc_{1.25}Ti_{1.25}Zr_{1.25})(Ge_{1.55}Ru_{0.47}Si_{0.98})$, $(Nb_{1.4}ScTiZr_{1.6})(Ge_{1.6}Pt_{0.3}Si_{1.1})$, and $(Nb_{1.4}ScTiZr_{1.6})(Ge_{1.6}Ir_{0.3}Si_{1.1})$ with the respective VEC value of 4.234, 4.275, and 4.238. In each sample, the main phase of XRD pattern is well characterized by the Mn_5Si_3-type structure (see **Figure 4**). However, the atomic composition, deviating from the starting one, as shown in **Table 3**, indicates that Ru, Pt, or Ir atoms cannot replace the atoms at the Si site. The SEM images of these samples show the precipitation of impurity phases at the grain boundaries of hexagonal-shaped main phases (see **Figure 6(a)–(c)**). χ_{ac} (T) measurements of these Mn_5Si_3-type HEA do not show a superconducting signal down to 3 K.

4. Summary

We have carried out materials research on the fcc and the Mn_5Si_3-type HEA superconductors. In the study of fcc HEA superconductors, we employed the Nb element, taking into account that the inclusion of rather high T_c elements is advantageous. Although some Nb-containing samples showed dominant fcc phases, single-phase ones could not be obtained. While we have found several new Nb-containing HEA phases in the multi-phase samples, no superconductivity appeared in each HEA phase down to 3 K. Considering that the Nb element forms a bcc structure at room temperature, and there are only several examples of fcc-related Nb-based superconductors, the discovery of Nb-containing fcc HEA superconductors would be a hard task. For the Mn_5Si_3-type HEA samples, we have successfully confirmed the single phase in $(Nb_{1.25}Sc_{1.25}Ti_{1.25}Zr_{1.25})(Ge_{1.8}Si_{1.2})$ with VEC = 4. However, this HEA compound does not show the diamagnetic signal down to 3 K. Some Mn_5Si_3-type superconductors possess the VEC value of 4.25 or 4.375. Thus Ru, Ir, or Pt element was substituted at the Si site to increase VEC, resulting in the unsuccessful attempt. We need a strategy to adjust the VEC value for the Mn_5Si_3-type HEAs.

The conclusions regarding the manufacturing process or microstructure in HEA superconductors are bulleted below.

- If one wants to obtain a single-phase sample with bcc, hcp, or fcc type structure by the arc-melting method, it would be a rather hard task due to an appearance of secondary phase and/or of phase with a slightly different composition.

- Eutectic HEAs receive much attention due to the rich functions arising from the microstructures [53]. In some cases, eutectic superconductors show enhanced superconducting critical temperatures. Therefore, the study of the eutectic phase in HEA superconductors might be interesting.

- Mechanical alloying has been widely used to produce HEAs [54]. The mechanical alloying process is different from the arc-melting one. So this is another route to obtain single-phase HEA superconductors.

5. Future directions

The formation of single-phase fcc HEA is realized at VEC larger than 8.0. According to the Matthias rule of transition metal alloys, T_c at such a large VEC value is substantially reduced. Therefore, the measurement of physical properties at much lower than 3 K is desired. Because the synthesis of quinary alloy with the single-phase might be a hard task, research on ternary or quarternary fcc multicomponent superconductor would be necessary. In the research area of HEAs, the CALPHAD (calculation of phase diagram) method is rapidly used for the prediction of HEAs or the study of the phase relation between HEAs and other alloys. If the thermodynamic data of various compounds in the present Nb-containing multicomponent systems are sufficiently collected, the CALPHAD method will elucidate the stability of a HEA in this system. Thus, our results will greatly assist in the evaluation of the CALPHAD method in the future.

Nb_5Ir_3O, crystallizing into the Ti_5Ga_4-type structure, which is the ordered derivative of Mn_5Si_3-type structure, is well known as a two-band superconductor [41]. By substituting Pt into Ir, the crossover to single-band superconductivity is observed [44], which is a rare phenomenon. This result promotes us to investigate multisite HEA superconductors for further search of the crossover phenomenon, and the high-entropy state may be a new route of controlling the superconducting band. Another interesting aspect of HEA is the cocktail effect. In bcc HEA superconductors, we have shown that the peculiar enhancement of T_c by introducing the high-entropy state is not observed [28]. It would be interesting to pursue the cocktail effect of T_c in multisite HEAs.

Acknowledgements

J.K. is grateful for the support provided by Comprehensive Research Organization of Fukuoka Institute of Technology.

Conflict of interest

The authors declare no conflict of interest.

Author details

Jiro Kitagawa*, Naoki Ishizu and Shusuke Hamamoto
Department of Electrical Engineering, Faculty of Engineering, Fukuoka Institute of Technology, Fukuoka, Japan

*Address all correspondence to: j-kitagawa@fit.ac.jp

References

[1] Gao M C, Yeh J W, Liaw P K, Zhang Y. High-entropy alloys: fundamentals and applications Swizerland: Springer; 2015.

[2] Murty B S, Yeh J W, Ranganathan S, Bhattacharjee P P. High-Entropy Alloys. 2nd ed. Amsterdam: Elsevier; 2019.

[3] Yeh J W, Chen S K, Lin S J, Gan J Y, Chin T S, Shun T T, Tsau C H, Chang S Y. Nanostructured high-entropy alloys with multiple principal elements: Novel alloy design concepts and outcomes. Adv. Eng. Mater. 2004; 6:299-303. DOI: 10.1002/adem.200300567

[4] Otto F, Yang Y, Bei H, George E P. Relative effects of enthalpy and entropy on the phase stability of equiatomic high-entropy alloys. Acta Mater. 2013;61:2628-2638. DOI: 10.1016/j.actamat.2013.01.042

[5] Rost C M, Sachet E, Borman T, Moballegh A, Dickey E C, Hou D, Jones J L, Curtarolo S, Maria J P. Entropy-stabilized oxides. Nat. Commun. 2015;6:8485. DOI: 10.1038/ncomms9485

[6] Musicó B L, Gilbert D, Ward T Z, Page K, George E, Yan J, Mandrus D, Keppens V. The emergent field of high entropy oxides: Design, prospects, challenges, and opportunities for tailoring material properties. APL Materials 2020;8:040912. DOI: 10.1063/5.0003149

[7] Ying T, Yu T, Shiah Y-S, Li C, Li J, Qi Y, Hosono H. High-entropy van der Waals materials formed from mixed metal dichalcogenides, halides, and phosphorus trisulfides. J. Am. Chem. Soc. 2021;143:7042-7049. DOI: 10.1021/jacs.1c01580

[8] Marik S, Singh D, Gonano B, Veillon F, Pelloquin D, Bréard Y. Enhanced magnetic frustration in a new high entropy diamond lattice spinel oxide. Scr. Mater. 2020;186:366-369. DOI: 10.1016/j.scriptamat.2020.04.027

[9] Sun L, Luo Y, Ren X, Gao Z, Du T, Wu Z, Wang J. A multicomponent γ-type $(Gd_{1/6}Tb_{1/6}Dy_{1/6}Tm_{1/6}Yb_{1/6}Lu_{1/6})_2Si_2O_7$ disilicate with outstanding thermal stability. Mater. Res. Lett. 2020;8:424-430. DOI: 10.1080/21663831.2020.1783007

[10] Rao Z, Dutta B, Körmann F, Lu W, Zhou X, Liu C, Kwiatkowski da Silva A, Wiedwald U, Spasova M, Farle M, Ponge D, Gault B, Neugebauer J, Raabe D, Li Z. Beyond solid solution high-entropy alloys: tailoring magnetic properties via spinodal decomposition. Adv. Funct. Mater. 2021;31:2007668. DOI: 10.1002/adfm.202007668

[11] Quintana-Nedelcos A, Leong Z, Morley N A. Study of dual-phase functionalisation of NiCoFeCr-Al_x multicomponent alloys for the enhancement of magnetic properties and magneto-caloric effect. Mater. Today: Energy 2021;20:100621. DOI: 10.1016/j.mtener.2020.100621

[12] Jung C, Kang K, Marshal A, Gokuldoss Pradeep K, Seol J–B, Lee H M, Choi P–P. Effects of phase composition and elemental partitioning on soft magnetic properties of AlFeCoCrMn high entropy alloys. Acta Mater. 2019;171:31-39. DOI: 10.1016/j.actamat.2019.04.007

[13] BaBa K, Ishizu N, Nishizaki T, Kitagawa J. Magnetic and transport properties of new dual-phase high-entropy alloy FeRhIrPdPt. Materials 2021;14:2877. DOI: 10.3390/ma14112877

[14] Koželj P, Vrtnik S, Jelen A, Jazbec S, Jagličić Z, Maiti S, Feuerbacher M, Steurer W, Dolinšek J. Discovery of a superconducting high-entropy alloy. Phys. Rev. Lett. 2014;113:107001. DOI: 10.1103/PhysRevLett.113.107001

[15] Matthias B T. Empirical relation between superconductivity and the number of valence electrons per atom. Phys Rev 1955;97:74-76. DOI: 10.1103/PhysRev.97.74

[16] Collver M M, Hammond R H. Superconductivity in "amorphous" transition-metal alloy films. Phys Rev Lett 1973;30:92-95. DOI: 10.1103/PhysRevLett.30.92

[17] von Rohr F O, Winiarski M J, Tao J, Klimczuk T, Cava R J. Effect of electron count and chemical complexity in the Ta-Nb-Hf-Zr-Ti high-entropy alloy superconductor. Proc. Natl. Acad. Sci. 2016;113:E7144-E7150. DOI: 10.1073/pnas.1615926113

[18] von Rohr F O, Cava R J. Isoelectronic substitutions and aluminium alloying in the Ta-Nb-Hf-Zr-Ti high-entropy alloy superconductor. Phys. Rev. Mater. 2018;2:034801. DOI: 10.1103/PhysRevMaterials.2.034801

[19] Marik S, Varghese M, Sajilesh K P, Singh D, Singh R P. Superconductivity in equimolar Nb-Re-Hf-Zr-Ti high entropy alloy. J. Alloys Compd. 2018;769:1059-1063. DOI: 10.1016/j.jallcom.2018.08.039

[20] Ishizu N, Kitagawa J. New high-entropy alloy superconductor $Hf_{21}Nb_{25}Ti_{15}V_{15}Zr_{24}$. Res. Phys. 2019;13:102275. DOI: 10.1016/j.rinp.2019.102275

[21] Zhang X, Winter N, Witteveen C, Moehl T, Xiao Y, Krogh F, Schilling A, von Rohr F O. Preparation and characterization of high-entropy alloy $(TaNb)_{1-x}(ZrHfTi)_x$ superconducting films. Phys. Rev. Res. 2020;2:013375. DOI: 10.1103/PhysRevResearch.2.013375

[22] Harayama Y, Kitagawa J. Superconductivity in Al-Nb-Ti-V-Zr multicomponent alloy. J. Supercond. Nov. Magn. 2021 DOI:10.1007/s10948-021-05966-z

[23] Lee Y S, Cava R J. Superconductivity in high and medium entropy alloys based on MoReRu. Physica C 2019;566:1353520. DOI: 10.1016/j.physc.2019.1353520

[24] Marik S, Motla K, Varghese M, Sajilesh K P, Singh D, Breard Y, Boullay P, Singh R P. Superconductivity in a new hexagonal high-entropy alloy. Phys. Rev. Mater. 2019;3:060602(R). DOI: 10.1103/PhysRevMaterials.3.060602

[25] Liu B, Wu J, Cui Y, Zhu Q, Xiao G, Wu S, Cao G, Ren Z. Superconductivity in hexagonal Nb-Mo-Ru-Rh-Pd high-entropy alloys. Scr. Mater. 2020;182:109-113. DOI: 10.1016/j.scriptamat.2020.03.004

[26] Liu B, Wu J, Cui Y, Zhu Q, Xiao G, Wu S, Cao G-h, Ren Z. Structural evolution and superconductivity tuned by valence electron concentration in the Nb-Mo-Re-Ru-Rh high-entropy alloys. J. Mater. Sci. Technol. 2021; 85:11-17. DOI: 10.1016/j.jmst.2021.02.002

[27] Sun L, Cava R J. High-entropy alloy superconductors: Status, opportunities, and challenges. Phys. Rev. Mater. 2019;3:090301. DOI: 10.1103/PhysRevMaterials.3.090301

[28] Kitagawa J, Hamamoto S, Ishizu N. Cutting edge of high-entropy alloy superconductors from the perspective of materials research. Metals 2020;10:1078. DOI: 10.3390/met10081078

[29] Stolze K, Tao J, von Rohr F O, Kong T, Cava R J. Sc−Zr−Nb−Rh−Pd and Sc−Zr−Nb−Ta−Rh−Pd high-entropy alloy superconductors on a CsCl-type lattice. Chem. Mater. 2018;30:906-914. DOI: 10.1021/acs.chemmater.7b04578

[30] Stolze K, Cevallos F A, Kong T, Cava R J. High-entropy alloy superconductors on an α-Mn lattice. J. Mater. Chem. C

2018;6:10441-10449. DOI: 10.1039/C8TC03337D

[31] Wu J, Liu B, Cui Y, Zhu Q, Xiao G, Wang H, Wu S, Cao G, Ren Z. Polymorphism and superconductivity in the V-Nb-Mo-Al-Ga high-entropy alloys. Sci. China Mater. 2020;63:823-831. DOI: 10.1007/s40843-019-1237-5

[32] Mizuguchi Y. Superconductivity in high-entropy-alloy telluride $AgInSnPbBiTe_5$. J. Phys. Soc. Jpn. 2019;88:124708. DOI: 10.7566/JPSJ.88.124708

[33] Kasem M R, Hoshi K, Jha R, Katsuno M, Yamashita A, Goto Y, Matsuda T D, Aoki Y, Mizuguchi Y. Superconducting properties of high-entropy-alloy tellurides M-Te (M: Ag, In, Cd, Sn, Sb, Pb, Bi) with a NaCl-type structure. Appl. Phys. Express 2020;13:033001. DOI: 10.35848/1882-0786/ab7482

[34] Yamashita A, Jha R, Goto Y, Matsuda T D, Aoki Y, Mizuguchi Y. An Efficient way of increasing the total entropy of mixing in high-entropy-alloy compounds: a case of NaCl-type $(Ag,In,Pb,Bi)Te_{1-x}Se_x$ ($x = 0.0, 0.25, 0.5$) superconductors. Dalton Trans. 2020;49:9118-9122. DOI: 10.1039/D0DT01880E

[35] Liu B, Wu J, Cui Y, Zhu Q, Xiao G, Wu S, Cao G-h, Ren Z. Superconductivity and paramagnetism in Cr-containing tetragonal high-entropy alloys. J. Alloys Compd. 2021;869:159293. DOI: 10.1016/j.jallcom.2021.159293

[36] Mizuguchi Y, Kasem M R, Matsuda T D. Superconductivity in $CuAl_2$-type $Co_{0.2}Ni_{0.1}Cu_{0.1}Rh_{0.3}Ir_{0.3}Zr_2$ with a high-entropy-alloy transition metal site. Mater. Res. Lett. 2020:9;141-147. DOI: 10.1080/21663831.2020.1860147

[37] Kasem M R, Yamashita A, Goto Y, Matsuda T D, Mizuguchi Y. Synthesis of high-entropy-alloy-type superconductors $(Fe,Co,Ni,Rh,Ir)Zr_2$ with tunable transition temperature. J. Mater. Sci. 2021;56:9499-9505. DOI: 10.1007/s10853-021-05921-2

[38] Cort B, Giorgi A L, Stewart G R. Low temperature specific heats of H(NbIrO) and R(NbPtO). J. Low. Temp. Phys. 1982;47:179-185. DOI: 10.1007/BF00682027

[39] Waterstrat R M, Kuentzler R, Muller J. Structural instabilities and superconductivity in quasi-binary Mn_5Si_3-type compounds. J. Less Common Met. 1990;167:169-178. DOI: 10.1016/0022-5088(90)90302-Z

[40] Lv B, Zhu X Y, Lorenz B, Wei F Y, Xue Y Y, Yin Z P, Kotliar G, Chu C W. Superconductivity in the Mn_5Si_3-type Zr_5Sb_3 system. Phys. Rev. B 2013;88:134520. DOI: 10.1103/PhysRevB.88.134520

[41] Zhang Y, Wang B, Xiao Z, Lu Y, Kamiya T, Uwatoko Y, Kageyama H, Hosono H. Electride and superconductivity behaviors in Mn_5Si_3-type intermetallics. npj Quantum Materials 2017;2:45. DOI: 10.1038/s41535-017-0053-4

[42] Li S, Liu X, Anand V, Lv B. Superconductivity from site-selective Ru doping studies in Zr_5Ge_3 compound. New J. Phys. 2018;20:013009. DOI: 10.1088/1367-2630/aa9ccd

[43] Hamamoto S, Kitagawa J. Superconductivity in oxygen-added Zr_5Pt_3. Mater. Res. Express 2018;5:106001. DOI: 10.1088/2053-1591/aad9cf

[44] Xu Y, Jöhr S, Das L, Kitagawa J, Medarde M, Shiroka T, Chang J, Shang T. Crossover from multiple- to single-gap superconductivity in $Nb_5Ir_{3-x}Pt_xO$ alloys. Phys. Rev. B 2020;101:134513. DOI: 10.1103/PhysRevB.101.134513

[45] Corbett J D, Garcia E, Guloy A M, Hurng W M, Kwon Y U, Leon-Escamilla E A. Widespread interstitial chemistry of Mn_5Si_3-type and related phases. Hidden impurities and opportunities. Chem. Mater. 1998;10:2824-2836. DOI: 10.1021/cm980223c

[46] Kitagawa J, Hamamoto S. Superconductivity in $Nb_5Ir_{3-x}Pt_xO$. JPS Conf. Proc. 2020;30:011055. DOI: 10.7566/JPSCP.30.011055

[47] Miracle D B, Senkov O N. A critical review of high entropy alloys and related concepts. Acta Mater. 2017;122:448-511. DOI: 10.1016/j.actamat.2016.08.081

[48] Izumi F, Momma K. Three-dimensional visualization in powder diffraction. Solid State Phenom. 2007; 130:15-20. DOI: 10.4028/www.scientific.net/SSP.130.15

[49] Tsubota M, Kitagawa J. A necessary criterion for obtaining accurate lattice parameters by Rietveld method. Sci. Rep. 2017;7:15381. DOI: 10.1038/s41598-017-15766-y

[50] Giorgi A L, Szklarz E G, Storms E K, Bowman A L, Matthias B T. Effect of Composition on the superconducting transition temperature of tantalum carbide and niobium carbide. Phys. Rev. 1962;125:837-838. DOI: 10.1103/PhysRev.125.837

[51] Matthias B T. Transition temperatures of superconductors. Phys. Rev. 1953;92:874-876. DOI: 10.1103/PhysRev.92.874

[52] Otto F, Yang Y, Bei H, George E P. Relative effects of enthalpy and entropy on the phase stability of equiatomic high-entropy alloys. Acta Materialia 2013;61:2628-2638. DOI: 10.1016/j.actamat.2013.01.042

[53] Lu Y, Dong Y, Guo S, Jiang L, Kang H, Wang T, Wen B, Wang Z, Jie J, Cao Z, Ruan H, Li T. A promising new class of high-temperature alloys: Eutectic high-entropy alloys. Sci. Rep. 2015;4:6200. DOI: 10.1038/srep06200

[54] Vaidya M, Muralikrishna G M, Murty B S. High-entropy alloys by mechanical alloying: A review. J. Mater. Res. 2019;34:664-686. DOI: 10.1557/jmr.2019.37